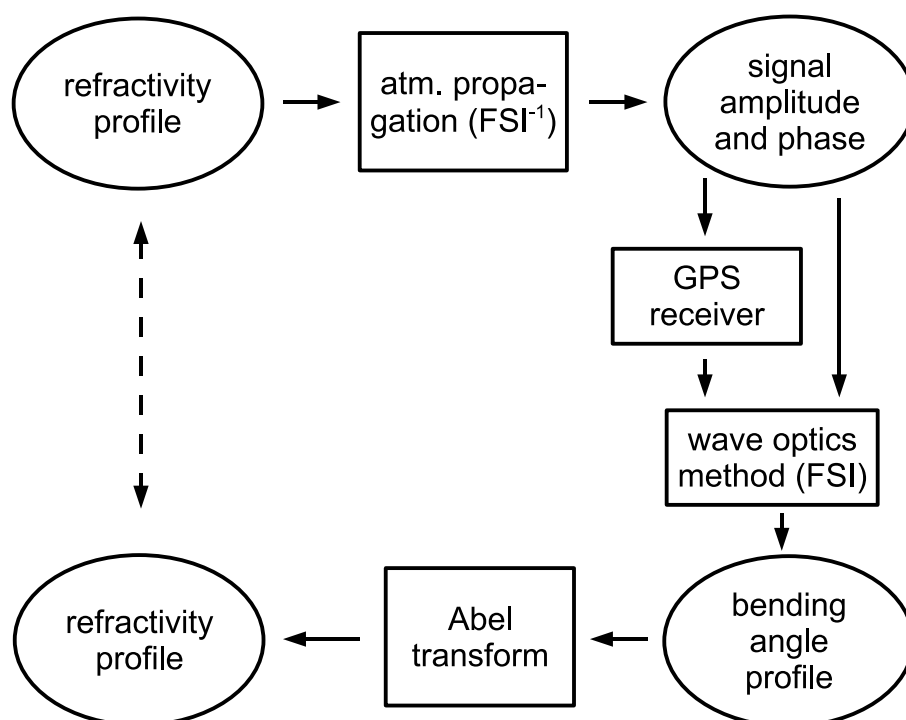


Scientific Report 05-09

Simulating GPS radio occultation events

Georg Beyerle

GFZ Potsdam, Germany, gbeyerle@gfz-potsdam.de





Colophone

Serial title:

Scientific Report 05-09

Title:

Simulating GPS radio occultation events

Subtitle:

Authors:

Georg Beyerle

GFZ Potsdam, Germany, gbeyerle@gfz-potsdam.de

Other Contributors:

Responsible Institution:

Danish Meteorological Institute

Language:

English

Keywords:

Url:

www.dmi.dk/dmi/dmi-publikationer.htm

ISSN:

1399-1949

ISBN:

87-7478-530-3

Version:

Website:

www.dmi.dk

Copyright:

Danish Meteorological Institute

Contents

Colophone	2
Contents	3
1 Introduction	6
2 LEO and GPS orbits	9
3 Refractivity profile	10
Analytical expression	10
Radio sonde data	10
4 Forward model	13
Inverse Abel transform	13
Multiple phase screens	14
Inverse FSI	14
5 Receiver model	16
Closed-loop tracking	17
Open-loop tracking	18
Fly-wheel mode tracking	19
Amplitude and residual phase	20
6 Data retrieval	23
Full Spectrum Inversion	23
Abel transform	24
7 Simulation results	26
8 Conclusions	28
References	29
A Installation	33
B Usage	33
C License	38

Simulating GPS radio occultation events

Georg Beyerle

GFZ Potsdam, Germany, gbeyerle@gfz-potsdam.de

Preface

This report describes the GPS radio occultation simulation tool SIMEND2END, its MATLAB implementation and usage, as well as the main processing algorithms and results from simulation studies. SIMEND2END's implementation has been finalized and a significant number of simulation runs have been performed when the author was GRAS SAF visiting scientist at the Danish Meteorological Institute in late spring 2005. A paper addressing the simulation study's principal results as well as a statistical analysis of radio sonde data concerning the occurrence of critical refraction was prepared and submitted for publication to the Journal of Geophysical Research (*Beyerle et al.*, 2005). The present report serves as a complement to this paper; the report's main focus is on the discussion of implementation details of the simulation tool. The analysis of critical refraction phenomena derived from the radio sonde observations and the corresponding simulation results is presented in the paper and only a summary is given here. As a consequence of the overlap between the focal points of the submitted paper and this report several figures and text sections found in the paper are reproduced here. A preprint of the paper and SIMEND2END's sources are available at <http://www.gfz-potsdam.de/pbl/staff/gbeyerle/>.

Abstract

Validation studies of atmospheric refractivity observed by the GPS radio occultation experiment aboard the CHAMP satellite identify significant biases and enhanced standard deviations in the lower troposphere at low latitudes. In order to separate bias contributions caused by critical refraction from contributions induced by the occultation receiver's signal tracking loops an end-to-end simulation tool was developed and implemented within the MATLAB programming environment. With a data set of 1992 refractivity profiles derived from high-resolution low-latitude radio sonde observations simulation studies including several closed-loop and open-loop signal tracking techniques were performed. The individual steps of the simulation processing chain and their underlying algorithms are described. The results from the simulation study show that a receiver model capable of fly-wheeling qualitatively reproduces the CHAMP observations, which are characterized by negative biases in the planetary boundary layer, enhanced standard deviations and frequent occurrences of loss of signal tracking lock in the lower troposphere. Closed loop tracking with reduced loop order is found to be a viable alternative to fly-wheeling and open-loop techniques.

Abbreviations

AWI	Alfred Wegener Institute for Polar and Marine Research, Bremerhaven
C/A code	coarse acquisition code
CHAMP	CHAllenging Minisatellite Payload (German geo-research satellite)
DMI	Danish Meteorological Institute, Copenhagen
ECMWF	European Centre for Medium-Range Weather Forecasts, Reading
FSI	full spectrum inversion
GFZ	GeoForschungsZentrum Potsdam, Germany
GPS	Global Positioning System
GPS/MET	GPS/Meteorology (proof-of-concept satellite mission)
LEO	low-Earth orbiting
MPS	multiple phase screen
NCO	numerically-controlled oscillator
P code	precise code
PBL	planetary boundary layer
PLL	phase-locked loop
RO	radio occultation

1. Introduction

Since March 2001 a Global Positioning System (GPS) radio occultation (RO) experiment aboard the CHAMP (CHALLENGING Minisatellite Payload) geo-research satellite (*Reigber et al.*, 2002, 2005) records signals from GPS satellites setting behind Earth's horizon. Since activation of the RO experiment on 11 February 2001 about three hundred thousand occultation events have been observed, about 64% of which could be successfully processed and converted to profiles of atmospheric temperature (*Wickert et al.*, 2001, 2004; *Hajj et al.*, 2004). As the signal propagates through the ionosphere and the neutral atmosphere its amplitude changes and its group and phase velocity deviates from the vacuum speed of light. From these characteristic carrier phase and amplitude changes the ray bending angle profile $\alpha(p)$ and, subsequently, the atmospheric refractivity profile $N(z) = (n(z) - 1) \cdot 10^6$ are derived (see e.g., *Melbourne et al.*, 1994; *Kursinski et al.*, 1997; *Yunck et al.*, 2000; *Hajj et al.*, 2002). Here, $n(z)$ denotes the real part of the atmospheric refractive index, p and z are the ray impact parameter and the altitude, respectively.

In the upper troposphere and lower stratosphere, at altitudes between about 7–8 km and 35 km, good agreement between CHAMP RO measurements and meteorological analyses is found. In the lower troposphere, however, validation studies of the CHAMP, as well as the earlier proof-of-concept GPS/MET mission report on significant negative refractivity biases on the order of several percent (*Rocken et al.*, 1997; *Wickert et al.*, 2004; *Marquardt et al.*, 2003; *Ao et al.*, 2003; *Hajj et al.*, 2004).

The N -bias may be attributed to two factors. First, for vertical refractivity gradients below a threshold value of $dN_c/dz \equiv 10^6/r_E \approx -157 \text{ km}^{-1}$ the local curvature of the ray exceeds the curvature of the refractive index field and the ray is either absorbed by the ground or refracted outside of the orbit sector in which the receiver records signals (*Ao et al.*, 2003; *Sokolovskiy*, 2003). In occultation events affected by critical refraction the retrieved bending angles and, subsequently, the retrieved refractivities are systematically smaller than the true values (*Sokolovskiy*, 2003). Second, the signal tracking process performed by the occultation receiver may induce carrier phase errors which also contribute to the refractivity bias (see e.g., *Gorbunov*, 2002; *Ao et al.*, 2003; *Beyerle et al.*, 2003). It is well established that the implementation of open-loop signal tracking techniques in future RO instruments will prevent the receiver from prematurely losing tracking lock and will provide access to carrier phase and amplitude data in the planetary boundary layer at low latitudes (*Sokolovskiy*, 2001b).

Negative biases in the lower troposphere are well-known from CHAMP and other satellite RO missions (see e.g. *Rocken et al.*, 1997; *Ao et al.*, 2003; *Hajj et al.*, 2004). Within an ensemble of retrieved refractivity profiles the exact shape of the fractional refractivity error depends also on the number of data points retrieved at a given altitude z , in the following denoted by $m(z)$; the loss-of-lock altitude $z_{50\%}$ refers to the altitude at which the number of successfully retrieved data points is reduced to 50%. If, e.g., more restrictive quality control criteria are employed removing outlier observations, $z_{50\%}$ increases correspondingly. If the fraction is above 50% within the full altitude range, $z_{50\%}$ is undefined. A plot of $m(z)$ is attached to the figures showing the fractional refractivity error $\Delta N/N_{true} \equiv (N - N_{true})/N_{true}$ in order to emphasize the mutual dependence between fractional refractivity error and $m(z)$.

The simulation tool SIMEND2END attempts to model GPS radio occultation events taking into account the receiver tracking process. Starting from a refractivity profile $N(z)$ the atmospheric propagation of a GPS signal is simulated with the inverse Full Spectrum Inversion (FSI) technique (*Gorbunov*, 2003; *Gorbunov and Lauritsen*, 2004). With the FSI method the simulated amplitude

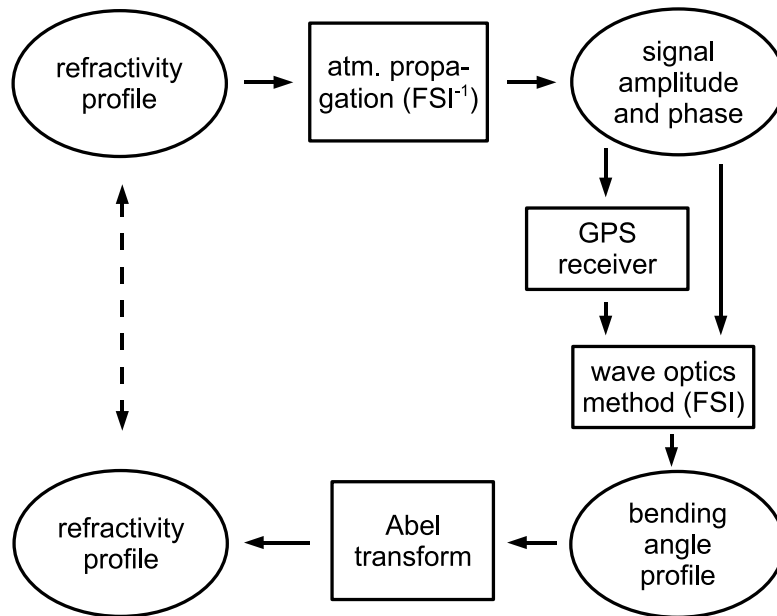


Figure 1.1: Schematic overview of the end-to-end simulation procedure.

and phase data are converted to bending angle profiles (*Jensen et al., 2003*). Finally, refractivity profiles are retrieved by Abel-transforming the bending angle profiles thereby closing the simulation loop (*Ao et al., 2003*). Optionally, a simplified signal receiver model can be inserted in the end-to-end simulation chain. Its schematic is shown in Figure 1.1.

Since the emphasis lies on statistical analysis of a large number of simulated retrieval results, we aim at a fast and efficient implementation. To achieve this objective a number of simplifying assumptions are made:

1. The orbits of the LEO and the occulting GPS are taken to be circular and coplanar.
2. The focus of the simulation tool is on the troposphere. Signal propagation through the ionosphere is not taken into account and only the signals at the L1 frequency (1.57542 GHz) are considered.
3. C/A and P code modulations are not explicitly simulated; the 50 Hz navigation data modulation is implemented as random sign changes every 20 ms.
4. Relativistic Doppler shifts and clock deviations are not included in the simulation.
5. In closed-loop tracking only the NCO frequency is updated, NCO phase update is not implemented. (*Stephens and Thomas, 1995*).
6. Atmospheric absorption is neglected, i.e. the imaginary part of the refractive index is assumed to vanish. (For a discussion of occultation data analysis for non-zero absorption see *Gorbunov and Kirchengast (2005)*.)

The occultation simulation tool SIMEND2END has been programmed and tested within the MATLAB programming environment (MATLAB version 7, version 5 and earlier versions are not supported). SIMEND2END's source files are located in the directory `.../simend2end/` and in the subdirectory `.../simend2end/private/`. Program flow is controlled by parameters stored in

the file `priv_controlpardefault.m` (default parameters) and the file `priv_controlparlocal.m` (site/machine specific parameters). Input data (e.g. radio sonde data) are read from `.../simend2end/data/in/`, results are stored as MATLAB-specific binary format data files in `.../simend2end/data/out/mat/`. Each simulation event is uniquely characterized by an occultation number `OccNo`, the type of signal tracking `TrackType`, and the carrier signal-to-noise density ratio `CN0` in units of dB Hz. The simulation results are visually displayed and/or stored in files for later analysis. Installation and usage of SIMEND2END is described in the appendices A and B (see also the file `readme` in the SIMEND2END distribution).

The outline of this report is as follows: in chapter 2 the calculation of GPS and LEO orbits are described, chapter 3 discusses the calculation and parameterization of the refractivity profile, which is used as input to the forward model, outlined in chapter 4. Chapter 5 focuses on the closed-loop and open-loop signal tracking receivers, the retrieval of bending angles and refractivities obtained from the receiver output is presented in chapter 6. Finally, results of the simulation study are summarized in chapter 7. The appendix includes SIMEND2END's installation and usage notes.

2. LEO and GPS orbits

The simulated satellite orbits are taken to be circular in order to improve the simulator's computational efficiency. The approximation is justified since CHAMP's and the GPS satellites' true orbit eccentricities are below 0.004 and 0.023, respectively, corresponding a deviation from a circular orbit of less than a few hundred meters and a few kilometers during the duration of an occultation event (about 100 s). In addition, Earth's local curvature radius is set to a fixed value at $r_E = 6,378.1363$ km. The LEO (low-Earth orbiting) and occulting GPS spacecrafts are assumed to be counterrotating within the same (occultation) plane; the LEO (occulting GPS) orbit radius and velocity are $r_L \equiv |\vec{r}_L| = 6800$ km and $v_L = 7.65$ km/s ($r_G = 26,800$ km and $v_G = 3.837$ km/s), respectively. With these values the temporal change of the satellite-to-satellite angle

$$\theta \equiv \arccos \left(\frac{\vec{r}_L \cdot \vec{r}_G}{r_L r_G} \right) \quad (2.1)$$

amounts to (a constant value of) $d\theta(t)/dt = 1.268 \cdot 10^{-3}$ rad/s.

Within SIMEND2END the orbit calculation of LEO and occulting GPS is performed by the private function `priv_leogpsorbits.m`. The function returns the structure `DataLv2` containing fields with position and velocity information at a sampling frequency of 50 Hz.

3. Refractivity profile

The refractivity profile is parameterized using a spline fit over a certain altitude interval. Above and below this interval the profile is extrapolated with a exponential function. The parameterization is initialized with a function call to `simend2endrefrpar_<OccNo>.m`. E.g. with `OccNo=17` the function `simend2endrefrpar_17.m` needs to exist in the MATLAB search path and should return a structure `RefrPar` containing the spline fit parameters. An analytical expression or observational data (radio sondes) can be used to initialize the refractivity profile.

Analytical expression

Following *Sokolovskiy* (2001a) we consider an exponential refractivity profile with a tropospheric disturbance.

$$N = N_0 \exp\left(-\frac{z}{H}\right) \left(1 - N_D \frac{2}{\pi} \arctan\left(\frac{z - z_D}{H_D}\right)\right) \quad (3.1)$$

The functions `simend2endrefrpar_1.m`, ..., `simend2endrefrpar_42.m` exemplify implementations of Eqn. 3.1 with disturbance amplitudes varying between $N_D = 0$ (no disturbance) and $N_D = 8$.

Fig. 3.1 shows the refractivity and vertical refractivity gradient for $N_0 = 400$ and a scale height $H = 8$ km. The disturbance is located at $z_D = 6$ km, with vertical extent of $H_D = 50$ m and amplitudes of $N_D = 1$ and $N_D = 2.5$.

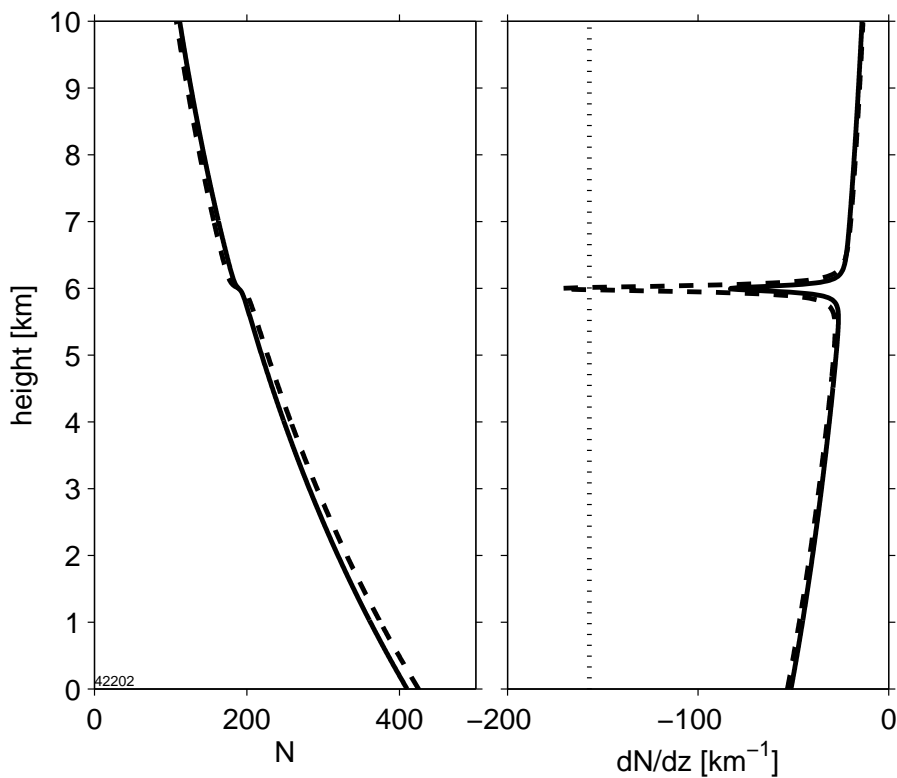


Figure 3.1: Vertical profiles of refractivity (left panel) and the corresponding refractivity gradient (right) derived from Eqn. 3.1 for disturbances of $N_D = 1$ (solid line) and $N_D = 2.5$ (dashed). The critical value of -157 km^{-1} is marked as dotted line.

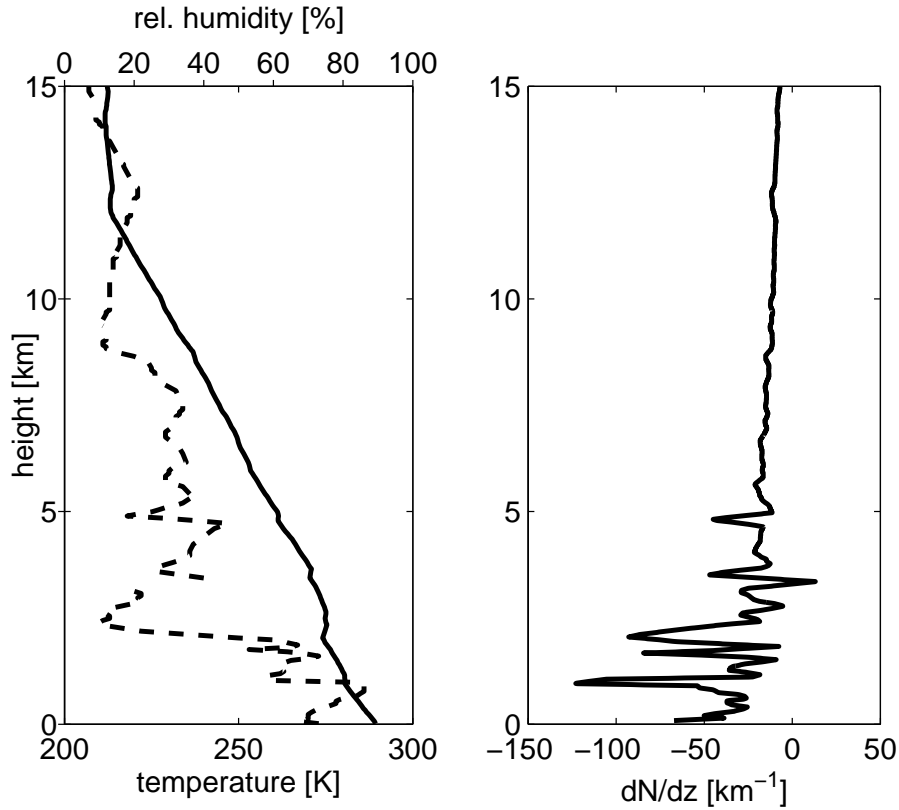


Figure 3.2: Radio sonde profile observed by Alfred Wegener Institute aboard RV “POLARSTERN” at 29.9°N, 14.6°W on 2 January 1983 (profile ID #10).

Radio sonde data

Occultation numbers $100000 \leq \text{OccNo} \leq 199999$ are reserved for refractivity profiles extracted from radio sonde data collected aboard RV “POLARSTERN” by Alfred Wegener Institute for Polar and Marine Research, Bremerhaven (AWI) mostly on the Atlantic ocean. AWI’s sonde data archive is accessible through

<http://www.awi-bremerhaven.de/MET/Polarstern/raso.html>.

From the observed pressure $p(z)$, water vapour partial pressure $p_w(z)$ and temperature profiles $T(z)$ refractivity $N \equiv 10^6 (n - 1)$ is calculated using (Thayer, 1974)

$$N = k_1 \frac{p - p_w}{T} + k_2 \frac{p_w}{T} + k_3 \frac{p_w}{T^2} \quad (3.2)$$

with n denoting the real part of the atmospheric refractive index and $k_1 = 0.7760$ K/Pa, $k_2 = 0.648$ K/Pa and $k_3 = 3.776 \cdot 10^3$ K²/Pa. For simplicity the difference between geopotential and geometric height is neglected in the simulation. Above the balloon burst height z_B the refractivity profile is extrapolated exponentially

$$N(z) = N(z_B) \exp\left(-\frac{z - z_B}{H}\right) \quad \text{for } z > z_B \quad (3.3)$$

with a scale height of $H = 7$ km (default value).

The refractivity profiles are linearly interpolated on an altitude grid with 5 m resolution and low-pass filtered using a running mean with 150 m width (adjustable via the parameter

Control.SondeProfileSmooth) to reduce measurement noise introduced by the humidity sensor (Vaisala, 1989). Refractivity for arbitrary values of z are obtained from spline fit parameters stored in the structure RefrPar using the function `priv_calcrefractivity.m`.

In the following the individual steps of the simulation process are illustrated with one particular sonde observation from the AWI radio sonde data set, measured aboard RV “POLARSTERN” at 29.9°N, 14.6°W on 2 January 1983 (profile ID #10). Fig. 3.2 shows the corresponding temperature and relative humidity profiles (left panel) together with the derived vertical refractivity gradient (right panel). In the planetary boundary layer (PBL) below 2 km altitude strong gradients causing multipath beam propagation are observed. However, the threshold value for the occurrence of critical refraction $dN_c/dz = -157 \text{ km}^{-1}$ is not reached.

4. Forward model

The forward model translates the refractivity profile $N(z)$ into a bending angle profile $\alpha(p)$ and, subsequently, $\alpha(p)$ into a time series of amplitude and phase path samples. This time series corresponds to a signal transmitted by the occulting GPS satellite following the orbit $\vec{r}_G(t)$ and recorded by an occultation receiver onboard the LEO moving along $\vec{r}_L(t)$.

Inverse Abel transform

If the refractivity field is spherically symmetric, i.e. $N(\vec{r}) = N(r)$, the inverse Abel transform relates the bending angle $\alpha(p)$ to the refractivity profile $N(r)$ (Fjeldbo *et al.*, 1971)

$$\alpha(p) = -2p \int_p^\infty \frac{dx}{\sqrt{x^2 - p^2}} \frac{d \ln(n(x))}{dx} \quad (4.1)$$

where $n = 1 + 10^{-6} N$ denotes the real part of the refractive index. Note that the integration is performed in impact parameter space.

Fig. 4.1 shows the derived bending angle as a function of ray height $p - r_E$, where r_E denotes the local curvature radius. Below ray heights of about 6 km multipath signal propagation generates characteristic bending angle fluctuations (Gorbunov and Gurvich, 1998; Gorbunov, 2002).

The inverse Abel transform is implemented in function `refrindex2bendangle_abel.m`. To capture the small-scale variability in the lower troposphere vertical resolution (parameter `Control.ABLVertResolution`) is reduced to 1 m below 6 km altitude (parameter

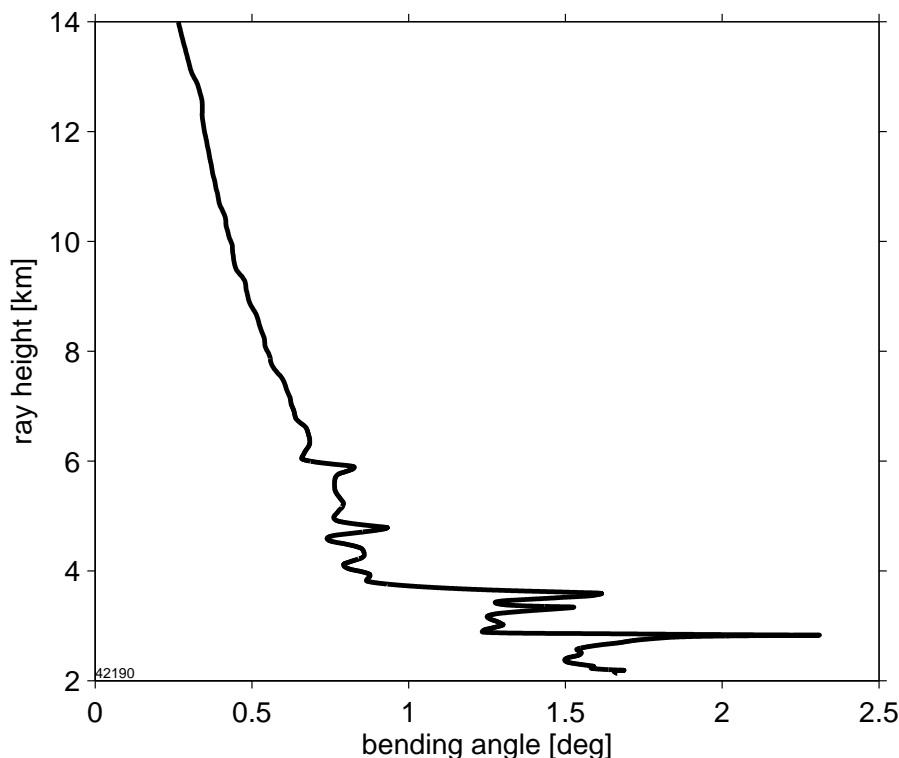


Figure 4.1: Bending angle profile derived from sonde observation ID #10.

Control.ABLHeightCritRefr) increasing to about 70 m at 150 km altitude (parameter Control.ABLMaxHeight). The corresponding parameters are initialized in function `priv_controlpardefault.m`

```
Control.ABLNofLevels      = 9001;    % number of altitude levels
Control.ABLHeightCritRefr = 6e3;    % upper end of high
                          % resolution range [m]
Control.ABLVertResolution = 1;      % vertical resolution
                          % below ABLHeightCritRefr [m]
Control.ABLMinHeight      = 0;      % minimum height range [m]
Control.ABLMaxHeight      = 150e3;  % maximum height range [m]
```

Multiple phase screens

If, on the other hand, the refractivity field deviates from spherical symmetry the inverse Abel transform (Eqn. 4.1) is not applicable. An efficient derivation of the bending angle $\alpha(p)$ for non-spherical refractivity fields provides the Multiple Phase Screen (MPS) technique (*Karayel and Hinson, 1997; Gorbunov and Gurvich, 1998; Sokolovskiy, 2001a*). In the MPS approach the refractivity field is modeled by a series of parallel phase screens. In our implementation the wave field is described by 20,000 rays propagating through $N_{ps} = 2001$ plane-parallel phase screens separated by $\Delta x = 1$ km. At each phase screen the incident wave suffers a phase shift whereas the wave's amplitude remains unchanged; between screens the wave is propagated through vacuum (*Gorbunov et al., 1996*). At the i^{th} phase screen the ray corresponding to impact parameter p is deflected by an angle $10^{-6} dN^{(i)}(z)/dz \Delta x$ where $N^{(i)}(z)$ denotes the refractivity profile on the i^{th} screen. The bending angle then follows from the summation over all phase screens

$$\alpha(p) \approx 10^{-6} \sum_{i=1}^{N_{ps}} \frac{dN^{(i)}(z(p))}{dz} \Delta x . \quad (4.2)$$

The MPS calculation is implemented in function `priv_mpspropagate.m`. The default parameters defining the number of rays, the number of screens and their separation are initialized in `priv_controlpardefault.m`

```
Control.MPSNofRays       = 20000;  % number of rays
Control.MPSNofScreens    = 2001;   % number of phase screens
Control.MPSScreenDist    = 1000;   % distance between screens [m]
```

respectively.

Inverse FSI

Individual rays within regions of multipath propagation can be disentangled by a transformation of the wave field in geometric space, $u(t)$, to a representation in impact parameter space, $U(p)$, from which the bending angle profile $\alpha(p)$ follows (*Gorbunov, 2001; Jensen et al., 2003*). Conversely, an inverse transformation relates $\alpha(p)$ to the signal in the time domain,

$$u(t) \equiv a(t) \exp(i\varphi(t)) \quad (4.3)$$

where $a(t)$ and $\varphi(t)$ denote the signal's amplitude and phase, respectively. The satellite-to-satellite angle $\theta(p)$ as a function of impact parameter p is related to the bending angle profile through

$$\theta(p) = \alpha(p) + \text{acos} \left(\frac{p}{r_L} \right) + \text{acos} \left(\frac{p}{r_G} \right). \quad (4.4)$$

For spherical LEO and GPS orbits $r_L = \text{const} = r_G$ and $\dot{\theta} \equiv d\theta(t)/dt = \text{const}$; thus, the Doppler angular frequency $\omega(p)$ is proportional to the impact parameter (*Jensen et al., 2003*),

$$\omega(p) = k \dot{\theta} p. \quad (4.5)$$

Signal phase and amplitude in impact parameter space, $\Phi(p)$ and $A(p)$, are obtained from (*Gorbunov and Lauritsen, 2004*)

$$\begin{aligned} \Phi(p) &= - \int d\omega t(\omega) = -k \int dp' \theta(p') \\ A(p) &\approx \sqrt{\frac{p}{r_L r_G \sin(\theta) \sqrt{r_L^2 - p^2} \sqrt{r_G^2 - p^2}}} \end{aligned} \quad (4.6)$$

and the signal $u(t)$ from the Fourier transform

$$u(t) = \mathcal{F}[U(p)] = \mathcal{F}[A(p) \exp(i \Phi(p))] \quad (4.7)$$

with amplitude and phase

$$\begin{aligned} a(t) &= |u(t)| \\ \varphi(t) &= \arg(u(t)). \end{aligned} \quad (4.8)$$

Fig. 4.2 shows the amplitude and Doppler profile that corresponds to the bending angle profile plotted in Fig. 4.1; for clarity an offset of 42 kHz has been subtracted from the Doppler profile. Multipath propagation causes significant amplitude and Doppler fluctuations starting at about 65 s occultation time.

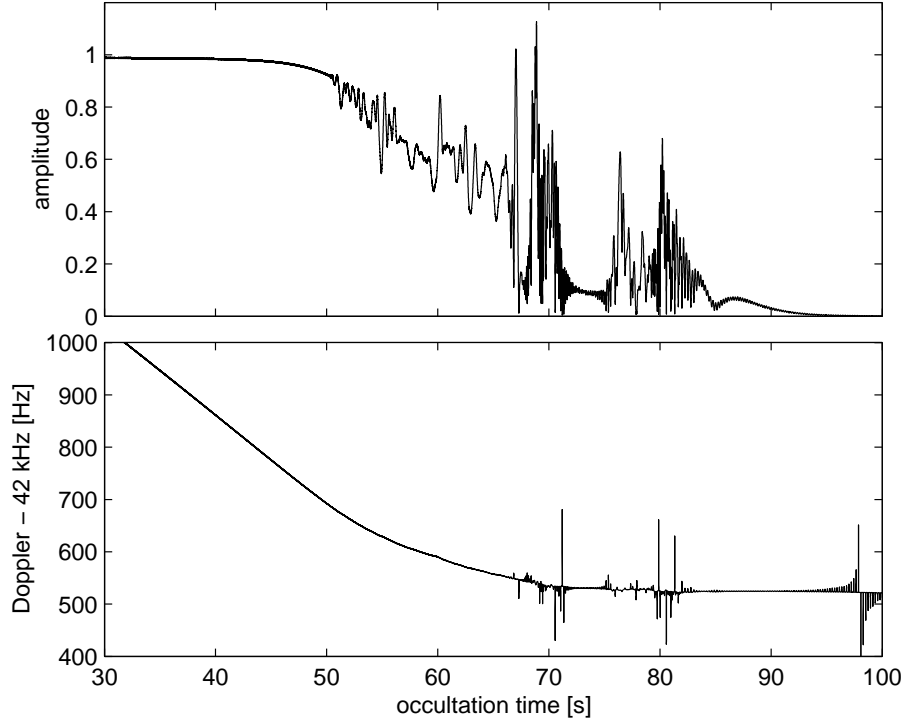


Figure 4.2: Simulated signal amplitude (top panel) and Doppler frequency profile (bottom) derived from sonde observation ID #10.

5. Receiver model

The receiver tracks the signal $u(t)$ by correlating $u(t)$ with replica signals

$$v^i(t) \equiv \cos[\Phi^{NCO}(t)] \quad \text{and} \quad v^q(t) \equiv -\sin[\Phi^{NCO}(t)]. \quad (5.1)$$

The replicas $v^i(t)$ and $v^q(t)$ are generated by the receiver's NCO (Kaplan, 1996; Tsui, 2000; Misra and Enge, 2002). In our simulation the NCO's frequency $f^{NCO}(t)$ is updated at a rate of $1/T = 1$ kHz, i.e. $f^{NCO}(t)$ is piecewise constant for $t_n \leq t < t_n + T$, $f_n^{NCO} \equiv f^{NCO}(t_n)$. Provided the amplitude $A(t)$ and frequency $f(t) \equiv 1/(2\pi) d\Phi/dt$ can be approximated as piecewise constant functions, $A_n \equiv A(t_n)$ and $f_n \equiv f(t_n)$, the inphase and quadphase correlation sums are given by

$$\begin{aligned} i_n &\equiv \frac{2}{T} \int_{t_n}^{t_n+T} u(t) v^i(t) dt + N_n^i \\ &\approx D_n A_n \frac{\sin(2\pi \Delta f_n T + \Delta\Phi_{n-1}) - \sin(\Delta\Phi_{n-1})}{2\pi \Delta f_n T} + N_n^i \end{aligned} \quad (5.2)$$

and

$$\begin{aligned} q_n &\equiv \frac{2}{T} \int_{t_n}^{t_n+T} u(t) v^q(t) dt + N_n^q \\ &\approx D_n A_n \frac{-\cos(2\pi \Delta f_n T + \Delta\Phi_{n-1}) + \cos(\Delta\Phi_{n-1})}{2\pi \Delta f_n T} + N_n^q, \end{aligned} \quad (5.3)$$

respectively, with $D_n \equiv D(t_n)$. Here, $\Delta f_n \equiv f_n - f_n^{NCO}$ and $\Delta\Phi_n \equiv \Phi_n - \Phi_n^{NCO}$ denote the difference between the true and the NCO frequency and the difference between the true and the

NCO phase, respectively. The NCO phase follows from

$$\Phi_n^{NCO} \equiv 2\pi T \sum_{j=1}^n f_j^{NCO} . \quad (5.4)$$

We note that Φ_n^{NCO} and Φ_n are accumulated phases and not restricted to the interval $[-\pi, +\pi]$. Gaussian white noise, N_n^i and N_n^q , with zero mean and standard deviations

$$\sigma(N_n^{i,q}) = \frac{A^{(0)}}{\sqrt{2T 10^{C/N_0/10}}} \quad (5.5)$$

is added to the correlation sums, i_n and q_n (Eqns. 5.2 and 5.3), where $A^{(0)}$ denotes the amplitude for vacuum propagation and C/N_0 is the noise carrier-to-density ratio expressed in dB Hz (*Kaplan*, 1996).

The total accumulated phase is the sum of NCO phase Φ_n^{NCO} and residual phase Φ_n^R (see section 5.4)

$$\varphi_n^{Rcv} = \Phi_n^{NCO} + \Phi_n^R . \quad (5.6)$$

Finally, output data volume is compressed from $1/T = 1$ kHz to 50 Hz by coherent summation over $K = 20$ samples

$$\begin{aligned} I_k &= \sum_{j=K \cdot (k-1)+1}^{K \cdot k} i_j \\ Q_k &= \sum_{j=K \cdot (k-1)+1}^{K \cdot k} q_j \\ \Phi_k^{Rcv} &= \frac{1}{K} \sum_{j=K \cdot (k-1)+1}^{K \cdot k} \varphi_j^{Rcv} . \end{aligned} \quad (5.7)$$

In the following, I_k and Q_k are denoted as coherent inphase and quadphase correlation sums, respectively. We note that Eqn. 5.7 implies a linear fit through φ_j^{Rcv} to obtain Φ_k^{Rcv} , *Thomas* (1989) discusses more sophisticated alternatives. From the coherent correlation sums the signal amplitudes

$$A_k^{Rcv} = \sqrt{(I_k)^2 + (Q_k)^2} \quad (5.8)$$

are obtained. Signal tracking is accomplished in either closed-loop or open-loop mode. The two modes will be discussed in section 5.1 and 5.2.

The simulation receiver is implemented with the functions `priv_tracking.m` (driver routine), `priv_tracksngnpllrateonly.m` (closed-loop and fly-wheeling tracking routine) and `priv_tracksngnopenloop.m` (open-loop tracking routine). First, with a call to `priv_navdatamodulation.m` 50 Hz data modulation is added to the signal in `priv_tracking.m`. For simplicity the navigation data is modelled as random bits. The modulated signal is tracked either in closed-loop, fly-wheeling or open-loop mode depending on the values of the parameters `Control.TrackClosedLoop`, `Control.FlyWheeling` and `Control.TrackClosedLoop`. The simulation receivers operate with an update frequency of 1 kHz; down-sampling from 1 kHz to (typically) 50 Hz output frequency (parameter `Control.OutputRate`) is performed by the function `priv_downsamplesignal.m`.

Closed-loop tracking

In closed-loop mode the NCO frequency is adjusted every C/A code period (about 1 ms) by $\delta f_{n+1}^{NCO} \equiv f_{n+1}^{NCO} - f_n^{NCO}$. The adjustments at interval $n + 1$ are given by

$$\delta f_{n+1}^{NCO} = \frac{1}{T} \left(\frac{K_1^{(2)} + K_2^{(2)}}{2\pi} \Phi_n^R + \frac{-K_1^{(2)}}{2\pi} \Phi_{n-1}^R \right) \quad (5.9)$$

(second order loop) or

$$\delta f_{n+1}^{NCO} = \delta f_n^{NCO} + \frac{1}{T} \left(\frac{K_1^{(3)} + K_2^{(3)} + K_3^{(3)}}{2\pi} \Phi_n^R + \frac{-2K_1^{(3)} - K_2^{(3)}}{2\pi} \Phi_{n-1}^R + \frac{K_1^{(3)}}{2\pi} \Phi_{n-2}^R \right) \quad (5.10)$$

(third order loop), respectively, where the residual phase Φ_n^R is given in radian and $K_1^{(2)} = 7.358 \cdot 10^{-2}$, $K_2^{(2)} = 2.810 \cdot 10^{-3}$ for a standard-underdamped second order loop with bandwidth of 30 Hz and $K_1^{(3)} = 7.172 \cdot 10^{-2}$, $K_2^{(3)} = 2.383 \cdot 10^{-3}$, $K_3^{(3)} = 3.020 \cdot 10^{-5}$ for a standard-underdamped third order loop with bandwidth of 30 Hz (*Stephens and Thomas, 1995*). For a reduced loop bandwidth of 5 Hz the corresponding third order loop parameters are $K_1^{(3)} = 1.283 \cdot 10^{-2}$, $K_2^{(3)} = 7.365 \cdot 10^{-5}$ and $K_3^{(3)} = 1.590 \cdot 10^{-7}$. With δf_{n+1}^{NCO} the NCO frequency of the $(n + 1)$ th update interval follows from $f_{n+1}^{NCO} = \delta f_{n+1}^{NCO} + f_n^{NCO}$ and subsequently i_{n+1} and q_{n+1} are calculated using Eqns. 5.4, 5.2 and 5.3.

Closed-loop tracking with and without fly-wheeling is implemented within the function `priv_tracksnpllrateonly.m`. To simplify signal acquisition the loop's NCO frequency is initialized with the true frequency and the noise component is gradually increased from zero to 100% over a time period of `Control.NoiseRiseTime` seconds (default value: 10 s). Optionally (if `Control.DataWipeActive` non-zero), data-wipe is applied; data-wipe is mandatory for `atan2()` (four quadrant) phase extraction.

Under the assumption that the signal amplitude and frequency remains constant over one C/A code period (about 1 ms) signal tracking is efficiently implemented with the "sin(x)/x" model (Eqns. 5.2/5.3 and *Ao et al. (2003)*). The accumulated NCO phase `PhsNCO` increases every `TUpd = 1 ms` by $2\pi \text{FrqNCO} \text{TUpd}$, and NCO frequency `FrqNCO` is adjusted every millisecond by the value `CarFrqOfsNew`, which is calculated by the nested function `nested_adjustNCOfrequency()` in `priv_tracksnpllrateonly.m`. The nested function `nested_adjustNCOfrequency()` yields the necessary frequency change that aligns the NCO with observed frequency.

Open-loop tracking

Open-loop tracking is commonly considered a possible solution to the problem of premature loss of lock in closed-loop receivers (*Sokolovskiy, 2001b*). In open-loop mode the loop feedback δf_{n+1}^{NCO} is calculated from a Doppler model $f^{model}(t_n) \equiv f_n^{model}$, i.e.

$$f_{n+1}^{NCO} = f_{n+1}^{model} \quad (5.11)$$

and therefore

$$\delta f_{n+1}^{NCO} = f_{n+1}^{model} - f_n^{NCO} \quad (5.12)$$

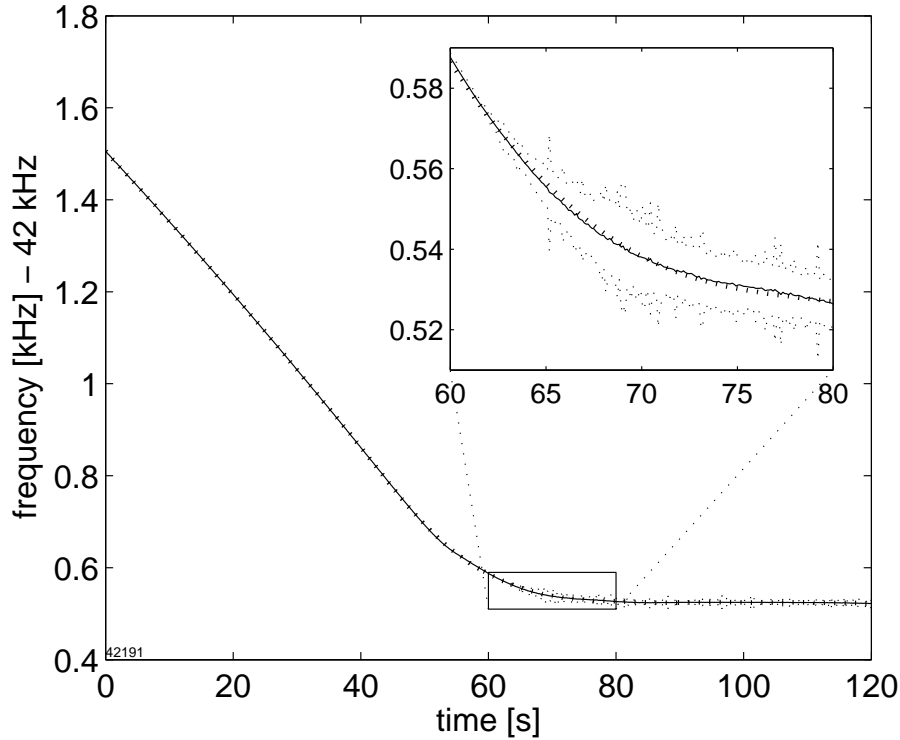


Figure 5.1: A-priori Doppler frequency profile used by the open-loop tracking model (thick dotted line). The mean Doppler profile and the corresponding 1σ standard deviations derived from the radio sonde data set are plotted as thin lines.

For simplicity, in this study the model f_n^{model} is taken to be ensemble average

$$f_n^{model} \equiv \frac{1}{N_R} \sum_{j=1}^{N_R} f_n^{(j)} \equiv \langle f_n^{(j)} \rangle \quad (5.13)$$

where $N_R = 1992$ and $f_n^{(j)}$ is the true signal frequency derived from the j th simulated Doppler profile at time interval n . The one-sigma standard deviation is about 10–20 Hz in good agreement with *Sokolovskiy* (2001b). Total phase is calculated from Eqn. 5.6, with Φ_n^R extracted from Eqn. 5.16 and Φ_n^{NCO} is derived from the NCO frequency (Eqn. 5.4). Analogous to the closed-loop case the sampling rate is reduced from 1 kHz to 50 Hz using Eqn. 5.7 and Eqn. 5.8 yields the signal amplitude.

Open-loop tracking is implemented with the function `priv_tracksgnopenloop.m`. The NCO frequency `FRQ_NCO` is calculated from the Doppler model, described by the parameter `OLFRQMD1` and initialized in function `priv_openloopfrqmodel.m`. The residual phase information is stored in the variables `TrkInphs` and `TrkQuadphs`, which are the inphase and quadphase correlation sums coherently integrated over 20 ms.

Fly-wheel mode tracking

The first occultation measurements from the proof-of-concept GPS/MET mission frequently suffered from loss of lock already in the upper or mid troposphere in particular at low latitudes (*Rocken et al.*, 1997). To solve this problem Jet Propulsion Laboratory developed and implemented the fly-wheeling tracking method (*Hajj et al.*, 2004). Fly-wheeling mode was successfully used in later phases of the GPS/MET mission and is the nominal tracking mode on the CHAMP and SAC-C satellites.

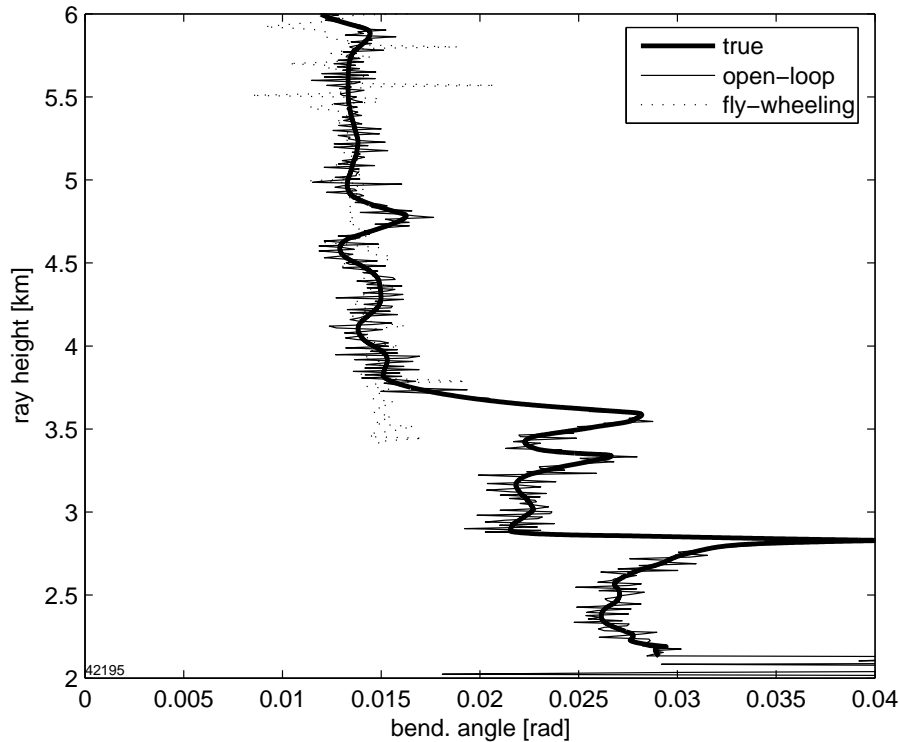


Figure 5.2: Bending angle profiles derived for carrier-to-noise density ratio of 40 dB Hz with open-loop and fly-wheeling signal tracking.

Fly-wheel tracking is activated when SNR_V drops below a predefined threshold value SNR_V^* . Once activated, the tracking loop is opened and f_{n+1}^{NCO} is calculated from the previous L NCO frequencies by extrapolating a polynomial fit through $f_{n-L+1}^{NCO}, \dots, f_n^{NCO}$. Thus, during fly-wheeling the carrier tracking loop is no longer phase-locked to the signal $u(t)$. The phasor $I + iQ$ starts to rotate freely in $I - Q$ space, effectively randomizing the residual phase values and causing significant phase errors. However, signal loss is less likely during fly-wheeling since large residual phase errors no longer cause f_n^{NCO} to shear out.

Our fly-wheeling simulations show that the results depend strongly on the selected fly-wheeling parameters: the number of samples L included in the polynomial fit, the degree of the extrapolation polynomial, the amplitude thresholds for activation and deactivation, possible time delays, etc. In our implementation the following parameters were found to give best results: $L = 2000$ corresponding to a time period of 2 s, a linear fit and a threshold value of $\text{SNR}_V^* = 40$. If the observed amplitude falls below SNR_V^* for more than 100 ms, fly-wheeling is activated. We stress that the design choices of our fly-wheeling implementation were made to achieve consistency with the CHAMP occultation data; the implementation should not be regarded as an accurate model of the “BlackJack” receiver aboard CHAMP.

Within closed-loop tracking (implemented in `priv_tracksnplrateonly.m`) fly-wheeling is activated if the parameter `Control.FlyWheeling` is non-zero. At each update step the threshold SNR_V^* is compared against the signal amplitude `FWAmplSqr`, coherently integrated over 20 ms. Evaluating the extrapolation polynomial with parameters `FWpp` at sample time k (using the function call `FrqNCO = polyval(FWpp, k, [], mu)`) yields the NCO frequency for the next time period. Note that `FWpp` is initialized solely during time periods of deactivated fly-wheeling.

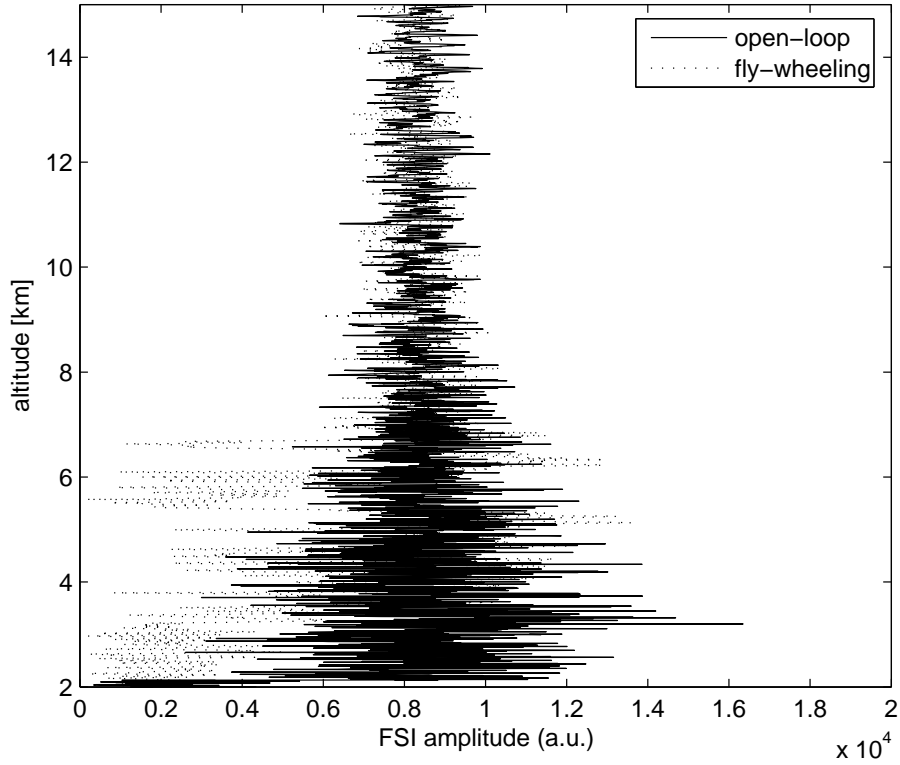


Figure 5.3: FSI amplitudes derived for carrier-to-noise density ratio of 40 dB Hz with open-loop and fly-wheeling signal tracking.

Amplitude and residual phase

The residual phases Φ_n^R (Eqn. 5.6) are extracted from the correlation sums (Eqns. 5.2 and 5.3) using

$$\Phi_n^R = \text{atan} \left(\frac{q_n}{i_n} \right) \quad (\text{two-quadrant phase extraction}) \quad (5.14)$$

or

$$\Phi_n^R = \text{atan2}(q_n, i_n) \quad (\text{four-quadrant phase extraction}). \quad (5.15)$$

In closed-loop mode the phase-locked loop (PLL) steers the residual phase Φ_n^R towards zero, i.e. $|i_n| \gg |q_n|$ if the tracking loop is locked to the signal. In open-loop mode (section 5.2), however, received and replica signals are no longer phase-locked, Φ_n^R possibly exceeds the interval $[-\pi, +\pi]$ and use of Eqn. 5.15 would introduce a cycle slip whenever Φ_n^R passes $\pm\pi$. These cycle slips are eliminated by adding the number of full cycles to Φ_n^R , i.e. Eqn. 5.15 is modified by

$$\Phi_n^R = \text{atan2}(q_n, i_n) + C_n \quad (5.16)$$

where

$$C_n = \begin{cases} C_{n-1} - 2\pi & : \text{atan2}(q_n, i_n) - \text{atan2}(q_{n-1}, i_{n-1}) < -\pi \\ C_{n-1} + 2\pi & : \text{atan2}(q_n, i_n) - \text{atan2}(q_{n-1}, i_{n-1}) > \pi \\ C_{n-1} & : \text{else} \end{cases} \quad (5.17)$$

and $C_1 = 0$.

In the current CHAMP occultation receiver closed-loop tracking with two-quadrant phase extraction is implemented (Ao *et al.*, 2003). With two-quadrant phase extraction the 50 Hz data modulation is

automatically taken care of, since Eqn. 5.14 is insensitive with respect to sign changes of i_n and q_n (Kaplan, 1996). Four-quadrant phase extraction, on the other hand, records the data modulation bits and introduces half-cycles whenever a bit transition occurs. Thus, four-quadrant phase extraction presupposes the removal of the 50 Hz data modulation prior to signal correlation (data demodulation or data wipe-off) and necessitates knowledge of the navigation message.

6. Data retrieval

The receiver outputs inphase / quadphase correlation sums and the NCO frequencies down-sampled from the receiver-internal 1 kHz update frequency to 50 Hz (typically). The output frequency is adjustable through the parameter `Control.OutputRate` (receiver output frequency in Hz). From the correlation sums signal phases and amplitudes are calculated.

Full Spectrum Inversion

The Full Spectrum Inversion technique allows for the calculation of bending angle profiles within regions of multipath ray propagation. Following *Jensen et al. (2003)*; *Gorbunov and Lauritsen (2004)* the bending angle $\alpha(p)$ is obtained from the satellite-to-satellite angle $\theta(p)$ (Eqn. 4.4)

$$\alpha(p) = \theta(p) - \arccos\left(\frac{p}{r_L}\right) - \arccos\left(\frac{p}{r_G}\right) . \quad (6.1)$$

$\theta(p)$ follows from the known function $\theta(t)$ provided t as a function of impact parameter, $t = t(p)$, can be determined. An inverse Fourier transform of the observed signal, $u(t) = a(t) \exp(i\varphi(t))$ with amplitude $a(t)$ and total phase $\varphi(t)$, yields

$$U(\omega) \equiv \mathcal{F}^{-1}[u(t)] = \mathcal{F}^{-1}[a(t) \exp(i\varphi(t))] \quad (6.2)$$

where $U(\omega) = A(\omega) \exp(i\Phi(\omega))$. As shown by *Jensen et al. (2003)*; *Gorbunov and Lauritsen (2004)*, for circular orbits a given angular frequency ω occurs just once during an occultation event and for such orbits it is sufficient to study $u(t)$. Thus, $t(\omega)$ is well defined and follows from the

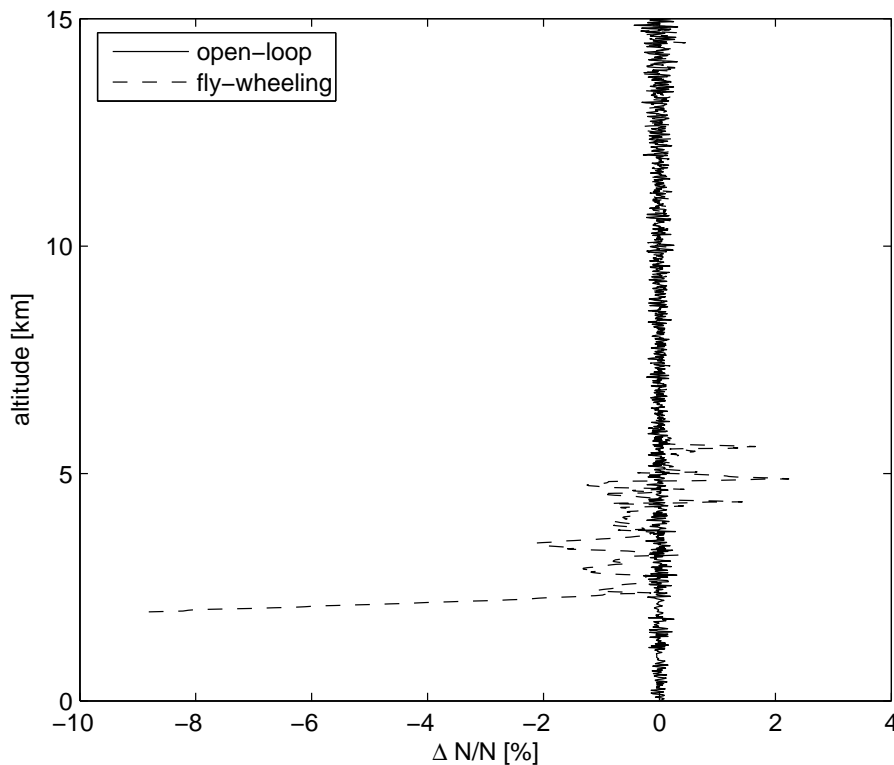


Figure 6.1: Fractional refractivity error derived for carrier-to-noise density ratio of 40 dB Hz with open-loop and fly-wheeling signal tracking.

transformed signal's phase (Eqn. 4.6),

$$\frac{d\Phi(\omega)}{d\omega} = -t(\omega) . \quad (6.3)$$

Using Eqn. 4.5 and $\theta = \dot{\theta} t$ ($\dot{\theta} = \text{const}$ for circular orbits) the satellite-to-satellite angle $\theta(p)$ can be calculated.

Within the FSI implementation (`priv_fullspectruminversion.m`) the independent variable, time t , is replaced by θ (*Jensen et al.*, 2003)

$$\theta = \frac{\omega}{k p} t . \quad (6.4)$$

For spherical orbits $\omega \propto p$ and, thus, $\theta \propto t$ and $\dot{\theta} = \omega / (k p)$.

Fourier transformation of the observed signal $u(\theta) = a(\theta) \exp(i \varphi(\theta))$ yields $U(\Omega) = A(\Omega) \exp(i \Phi(\Omega))$ with Ω denoting the angular “ θ -frequency”, the number of cycles per unit θ angle times 2π . Since multipath propagation is a tropospheric phenomenon (we ignore ionospheric multipath) the Fourier transformation can be restricted to $\theta > \theta^*$. The limit θ^* is chosen to correspond to a ray height of 30 km and is derived from a geometrical optic approximation.

Furthermore, the signal $u(t)$, recorded at 50 Hz and Doppler-shifted by about 40 kHz (Fig. 4.2), is under-sampled by a factor of about $40 \text{ kHz} / 50 \text{ Hz} = 800$. Nevertheless, (almost) no information is lost through aliasing provided the signal's bandwidth is less than the sampling frequency. The bandwidth in terms of angular θ -frequency is about

$$\Omega_{max} - \Omega_{min} \approx 2\pi / \dot{\theta} 300 \text{ Hz} \approx 1.5 \cdot 10^6 \text{ rad}^{-1} \quad (6.5)$$

for a tropospheric signal bandwidth of about 300 Hz (see Fig. 4.2). The receiver's 50 Hz sampling frequency corresponds to an angular sampling θ -frequency of $2\pi / \dot{\theta} / 50 \text{ Hz} \approx 2.5 \cdot 10^5 \text{ rad}^{-1}$. Thus, the signal $u(\theta)$ needs to be up-sampled by a factor of $1.5 \cdot 10^6 \text{ rad}^{-1} / 2.5 \cdot 10^5 \text{ rad}^{-1} = 6$. (With a receiver output rate of 300 Hz instead of 50 Hz this processing step could be eliminated.) The up-sampling is implemented in private function `priv_fullspectruminversion.m` as linear interpolation of amplitude $a(\theta)$ and accumulated phase $\varphi(\theta)$. The up-sampled signal is then shifted in Ω -space by Ω_{min} and Fourier transformed

$$\mathcal{F}^{-1}[u(\theta) \exp(i \Omega_{min} \theta)] = U(\Omega - \Omega_{min}) \quad (6.6)$$

where $U(\Omega) \equiv A(\Omega) \exp(i \Phi(\Omega))$. In analogy to Eqn. 6.3 the satellite-to-satellite angle in Ω -space is obtained from

$$\frac{d\Phi(\Omega)}{d\Omega} = -\theta(\Omega) \quad \text{i.e.} \quad \frac{\Phi_{i+1} - \Phi_i}{\Omega_{i+1} - \Omega_i} = -\theta_i \quad i = 1, \dots, M - 1 . \quad (6.7)$$

The phase Φ_i is extracted from the transformed signal, $\Phi_i = \arg(U(\Omega_i))$. To avoid aliasing we require $\delta\Phi \equiv |\Phi_{i+1} - \Phi_i| \lesssim \pi/2$. During a typical occultation event θ covers a range of about 0.1 rad; thus, $\delta\Omega \equiv |\Omega_{i+1} - \Omega_i| \approx \delta\Phi / 0.1 \text{ rad} \lesssim 15$. However, $\delta\Omega \lesssim 15$ implies that the full range in θ -space should be, $\theta_M - \theta_1 = 2\pi / \delta\Omega \gtrsim 0.42 \text{ rad}$, more than 4 times the observed range of 0.1 rad. Therefore, in the implementation of `priv_fullspectruminversion.m` the θ -range is expanded through zero-padding of $u(\theta)$ (*H.-H. Benzon, personal communication, 2005*).

Abel transform

If the refractivity field is spherically symmetric the refractive index follows from the bending angle $\alpha(p)$ by the Abel transform (Fjeldbo *et al.*, 1971)

$$n(r) = \exp \left(\frac{1}{\pi} \int_{p(r)}^{\infty} \frac{\alpha(p')}{\sqrt{p^2 - p'^2}} dp' \right). \quad (6.8)$$

Again, integration is performed in impact parameter space. Fig. 6.1 shows the deviation between fractional deviation between retrieved and input refractivity, $(N_{retr} - N_{true})/N_{true}$, for two receiver models, open-loop and fly-wheeling.

The Abel transform is implemented in the function `bendangle2refrindex_abel.m`. In `priv_fsigoimpactparsplce.m` the altitude resolution of the FSI bending angle profile is reduced to 10 m (adjustable through the parameter `Control.FSIAltResolution`). With 10 m vertical resolution numerical integration using the trapezoidal rule yields sufficient accuracy. At an altitude of 25 km (parameter `Control.FSIRayHeightXOver`) and above the FSI bending angle profile is replaced by the forward model result.

7. Simulation results

Three examples of end-to-end simulation results are presented in Figs. 7.1 to 7.3. A more detailed discussion is given in *Beyerle et al. (2005)*. The plots show the mean fractional difference between retrieved and true refractivity in the left panel (thick lines). Thin lines mark the one-sigma standard deviation. In addition, the number of retrieved data points as function of altitude is shown in the right panel. The true refractivity profiles are taken from 1992 radio sonde observations recorded and archived by AWI aboard RV “POLARSTERN” on the Atlantic ocean at latitudes between 30°S and 30°N. The simulations are performed for signal-to-noise density ratios of 40, 45 and 50 dB Hz.

The following three cases are considered:

1. The ideal receiver exactly reproduces the signal at its input; noise contributions are not included.
2. The reference receiver uses closed-loop tracking, two-quadrant phase extraction with a third order loop and 30 Hz loop bandwidth; this receiver model is capable of fly-wheeling. Qualitatively, this model corresponds to the current configuration of the “BlackJack” receiver aboard CHAMP.
3. The implementation of an open-loop receiver outputs inphase and quadphase correlation sums together with the phase model.

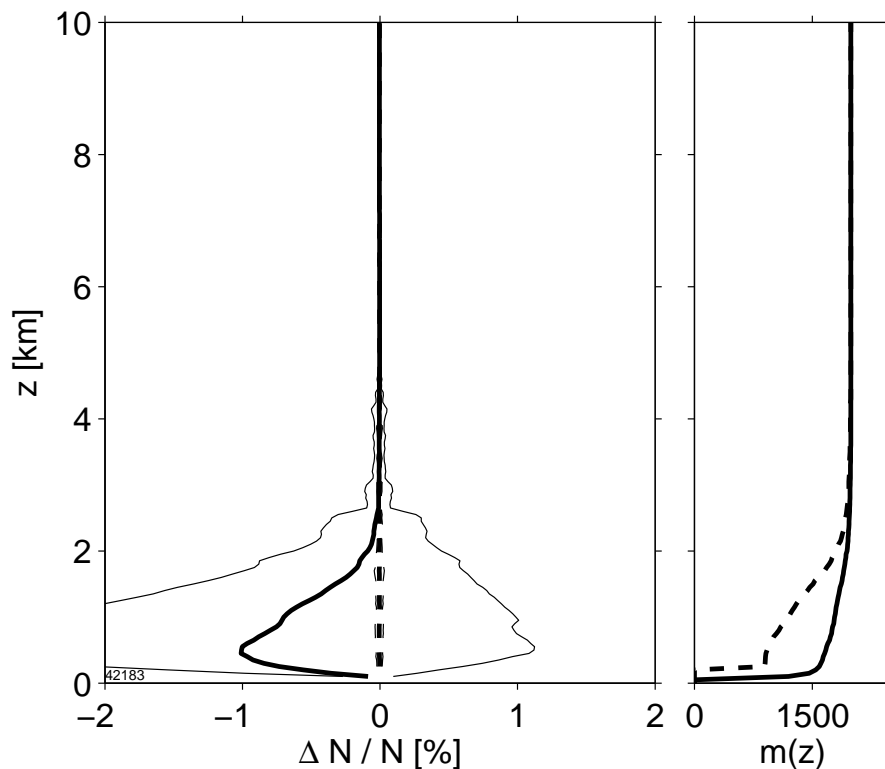


Figure 7.1: Left: fractional refractivity error derived from simulations using the ideal receiver is plotted as thick solid line. The thin lines indicate the one-sigma standard deviation. Excluding data affected by critical refraction yields an almost bias-free result (dashed lines). Right: number of retrieved data points. $z_{50\%}$ are 692 m and 99.5 m, respectively.

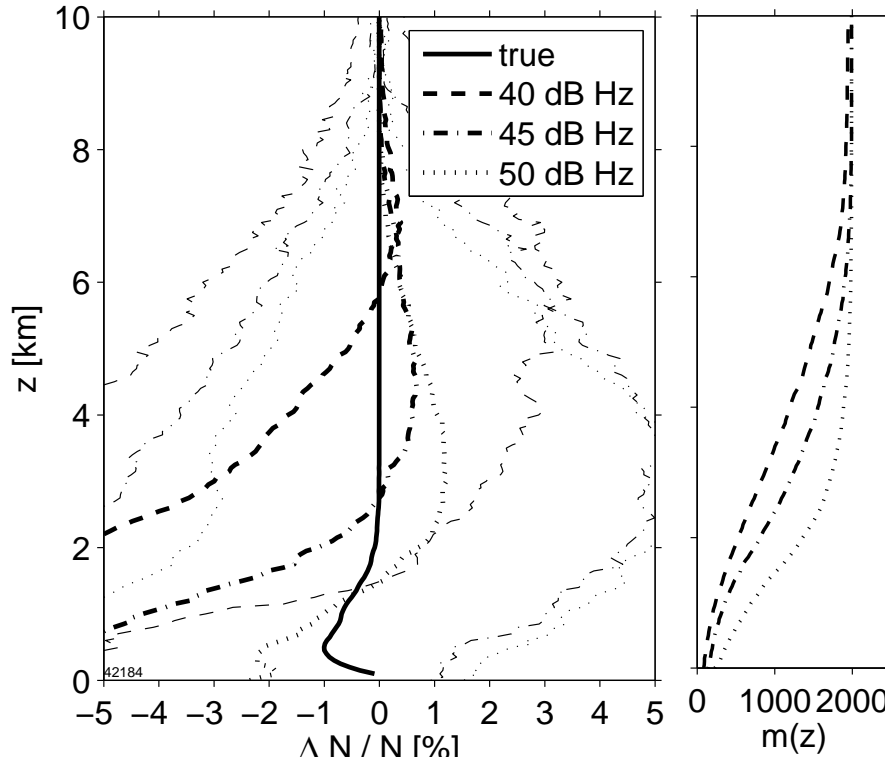


Figure 7.2: Same as Fig. 7.1, however signal is tracked in closed-loop mode with fly-wheeling enabled. $z_{50\%}$ are 3.4, 2.4 and 1.5 km for 40, 45 and 50 dB Hz, respectively.

The simulation results without signal tracking (ideal receiver) is plotted in Fig. 7.1. In a control run we restrict the comparison to the height range above $z_{CR} + 100$ m and obtain a mean fractional retrieval error and standard deviation below 0.01% and 0.03%, respectively (dashed lines). Here, z_{CR} denotes the largest altitude where critical refraction is observed. 58.3% of the radio sonde observations exhibit critical refraction with vertical refractivity gradients of less than -157 km^{-1} ; below 3 km this subset generates a negative bias of up to -1% and a standard deviation of about 2% (solid lines).

In the data analysis no quality control of outliers caused critical refraction has been performed in Figs. 7.2 and 7.3. The retrieval results may directly be compared to the ideal receiver profile (thick solid line in Fig. 7.1, left panel). For that purpose the solid line is repeated in both figures. The onset of a decrease in $m(z)$ already at 4–8 km altitude (Fig. 7.2, right panel) shows that the fly-wheeling receiver frequently loses tracking lock in the mid troposphere before reaching layers of critical refraction. Since loss of lock tends to occur at or above critical layers one would expect that the subset of successfully tracked signals minimizes the bias. However, a significant negative bias is observed below 5 km altitude. Within the PBL critical refraction might contribute to the negative N -bias; above 3 km receiver-induced errors are the most likely cause, since the occurrence of critical refraction above that altitude can be excluded.

The comparison between simulation results obtained by the open-loop receiver (Fig. 7.3) and results produced by the fly-wheeling receiver with two-quadrant phase extraction (Fig. 7.2) highlights the significant negative bias and enhanced standard deviation introduced by the latter. The open-loop refractivities (dashed, dashed-dotted and dotted lines in Fig. 7.3) exhibit almost no bias and reduced standard deviation with respect to the ideal receiver (solid line).

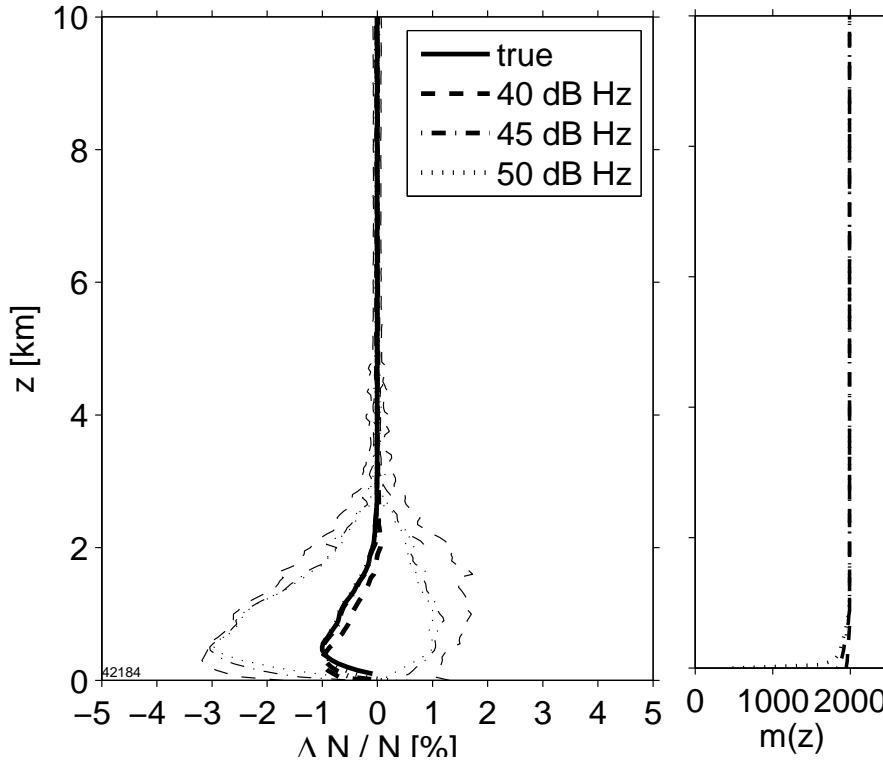


Figure 7.3: Same as Fig. 7.1, however signal is tracked in open-loop mode. $z_{50\%}$ is 0.023 km for 50 dB Hz.

8. Conclusions

The simulation tool SIMEND2END allows for the efficient simulation of GPS radio occultation events with different types of signal tracking techniques. The use of wave optical methods in the forward model and the inversion of the receiver-processed profiles guarantees the disentangling of interfering rays within regions of multipath propagation. The simulation reproduces on a qualitative level the tracking behavior of current fly-wheeling enabled receivers with two-quadrant phase extraction; in most occultation events the fly-wheeling receiver loses lock at or above the critical refraction layer. The results suggest that receivers using open-loop tracking will yield improvements in the mid and lower troposphere at altitude below 6–8 km in terms of retrieval bias, standard deviation and loss-of-lock altitude.

References

- Ao, C. O., T. K. Meehan, G. A. Hajj, A. J. Mannucci, and G. Beyerle (2003), Lower-troposphere refractivity bias in GPS occultation retrievals, *J. Geophys. Res.*, *108*(D18), 4577, doi:10.1029/2002JD003216.
- Beyerle, G., M. E. Gorbunov, and C. O. Ao (2003), Simulation studies of GPS radio occultation measurements, *Radio Sci.*, *38*(5), 1084, doi:10.1029/2002RS002800.
- Beyerle, G., T. Schmidt, J. Wickert, S. Heise, M. Rothacher, G. König-Langlo, and K. B. Lauritsen (2005), Observations and simulations of receiver-induced refractivity biases in GPS radio occultation, *J. Geophys. Res.*, submitted, preprint available at www.arxiv.org/physics/0502052.
- Fjeldbo, G., A. J. Kliore, and V. R. Eshleman (1971), The neutral atmosphere of Venus as studied with the Mariner V radio occultation experiments, *Astron. J.*, *76*(2), 123–140.
- Gorbunov, M. E. (2001), Radioholographic methods for processing radio occultation data in multipath regions, *scientific report 01-02*, Danish Meteorological Institute, Copenhagen, <http://www.dmi.dk/f+u/publikation/vidrap/2001/Sr01-02.pdf>.
- Gorbunov, M. E. (2002), Radio-holographic analysis of Microlab-1 radio occultation data in the lower troposphere, *J. Geophys. Res.*, *107*(D12), 4156, doi:10.1029/2001JD000889.
- Gorbunov, M. E. (2003), An asymptotic method of modeling radio occultations, *J. Atmos. Solar-Terr. Phys.*, *65*, 1361–1367, doi:10.1016/j.jastp.2003.09.001.
- Gorbunov, M. E., and A. S. Gurvich (1998), Microlab-1 experiment: Multipath effects in the lower troposphere, *J. Geophys. Res.*, *103*(D12), 13,819–13,826.
- Gorbunov, M. E., and G. Kirchengast (2005), Processing X/K band radio occultation data in the presence of turbulence, *technical report ESA/ESTEC No. 1/2005*, Inst. for Geophys., Astrophys., and Meteorol., University of Graz, Austria, Graz, <http://www.kfunigraz.ac.at/igam-arsclisys/publications/publ2005/MGorbandGKirc-LROTurbRep-IGAM-Mar05.pdf>.
- Gorbunov, M. E., and K. B. Lauritsen (2004), Analysis of wave fields by Fourier integral operators and their application for radio occultations, *Radio Sci.*, *39*, RS4010, doi:10.1029/2003RS002971.
- Gorbunov, M. E., A. S. Gurvich, and L. Bengtsson (1996), Advanced algorithms of inversion of GPS/MET satellite data and their application to reconstruction of temperature and humidity, *Report 211*, Max-Planck-Institut für Meteorologie, Germany, Hamburg.
- Hajj, G. A., E. R. Kursinski, L. J. Romans, W. I. Bertiger, and S. S. Leroy (2002), A technical description of atmospheric sounding by GPS occultation, *J. Atmos. Solar-Terr. Phys.*, *64*(4), 451–469.
- Hajj, G. A., et al. (2004), CHAMP and SAC-C atmospheric occultation results and intercomparisons, *J. Geophys. Res.*, *109*, D06109, doi:10.1029/2003JD003909.
- Jensen, A. S., M. Lohmann, H.-H. Benzon, and A. Nielsen (2003), Full spectrum inversion of radio occultation signals, *Radio Sci.*, *38*(3), 1040, doi:10.1029/2002RS002763.

- Kaplan, E. D. (1996), *Understanding GPS: Principles and applications*, Artech House, Boston, London.
- Karayel, E. T., and D. P. Hinson (1997), Sub-Fresnel-scale vertical resolution in atmospheric profiles from radio occultation, *Radio Sci.*, 32(2), 411–423.
- Kursinski, E. R., G. A. Hajj, J. T. Schofield, R. P. Linfield, and K. R. Hardy (1997), Observing Earth's atmosphere with radio occultation measurements using Global Positioning System, *J. Geophys. Res.*, 19(D19), 23,429–23,465.
- Marquardt, C., K. Schöllhammer, G. Beyerle, T. Schmidt, J. Wickert, and C. Reigber (2003), Validation and data quality of CHAMP radio occultation data, in *First CHAMP mission results for gravity, magnetic and atmospheric studies*, edited by C. Reigber, H. Lühr, and P. Schwintzer, pp. 384–396, Springer–Verlag, Berlin.
- Melbourne, W. G., E. S. Davis, C. B. Duncan, G. A. Hajj, K. R. Hardy, E. R. Kursinski, T. K. Meehan, L. E. Young, and T. P. Yunck (1994), The application of spaceborne GPS to atmospheric limb sounding and global change monitoring, *JPL Publication 94-18*, Jet Propulsion Laboratory, Pasadena, CA, USA.
- Misra, P., and P. Enge (2002), *Global positioning system: Signals, measurements, and Performance*, Navtech Seminars and GPS Supply, Suite 400, 6121 Lincolnia Rd., Alexandria, VA, USA.
- Reigber, C., H. Lühr, and P. Schwintzer (2002), CHAMP mission status, *Adv. Space Res.*, 30(2), 129–134.
- Reigber, C., H. Lühr, P. Schwintzer, and J. Wickert (2005), *Earth Observation with CHAMP: Results from Three Years in Orbit*, Springer–Verlag, Berlin Heidelberg New York.
- Rocken, C., et al. (1997), Analysis and validation of GPS/MET data in the neutral atmosphere, *J. Geophys. Res.*, 102(D25), 29,849–29,866.
- Sokolovskiy, S. V. (2001a), Modeling and inverting radio occultation signals in the moist troposphere, *Radio Sci.*, 36(3), 441–458.
- Sokolovskiy, S. V. (2001b), Tracking tropospheric radio occultation signals from low Earth orbit, *Radio Sci.*, 36(3), 483–498.
- Sokolovskiy, S. V. (2003), Effect of superrefraction on inversions of radio occultation signals in the lower troposphere, *Radio Sci.*, 38(3), 1058, doi:10.1029/2002RS002728.
- Stephens, S. A., and J. B. Thomas (1995), Controlled-root formulation for digital phase-locked loops, *IEEE Transactions on Aerospace and Electronic Systems*, 31(1), 78–95.
- Thayer, G. D. (1974), An improved equation for the radio refractive index of air, *Radio Sci.*, 9(10), 803–807.
- Thomas, J. B. (1989), An analysis of digital phase-locked loops, *JPL Publication 89-2*, Jet Propulsion Laboratory, Pasadena, USA.
- Tsui, J. B.-Y. (2000), *Fundamentals of Global Positioning System Receivers: A Software Approach*, 258 pp., John Wiley & Sons, Inc., New York.
- Vaisala (1989), Upper air systems: RS 80 radiosondes, *Tech. rep.*, Vaisala GmbH, Hamburg.

Wickert, J., T. Schmidt, G. Beyerle, R. König, C. Reigber, and N. Jakowski (2004), The radio occultation experiment aboard CHAMP: Operational data processing and validation of atmospheric parameters, *J. Meteorol. Soc. Jpn.*, 82(1B), 381–395.

Wickert, J., et al. (2001), Atmosphere sounding by GPS radio occultation: First results from CHAMP, *Geophys. Res. Lett.*, 28(17), 3263–3266.

Yunck, T. P., C.-H. Liu, and R. Ware (2000), A history of GPS sounding, *Terrestrial, Atmospheric and Oceanic Sciences*, 11(1), 1–20.

Acknowledgements

Financial support from EUMETSAT's GRAS SAF visiting scientist programme at DMI is gratefully acknowledged. I thank Kent Lauritsen, Georg Larsen, Hans-Henrik Benzon, Frans Rubek and Martin Sørensen for their friendly hospitality and many fruitful discussions. Enlightening conversations and debates with Magnus Bonnedal, Jacob Christensen, Axel von Engeln, Michael Gorbunov, Stefan Heise, Gert König-Langlo, Arne Jensen, Chris Marquardt, Tom Meehan, Torsten Schmidt, Sergey Sokolovskiy and Jens Wickert are gratefully acknowledged. Alfred Wegener Institute for Polar and Marine Research, Bremerhaven provided radio sonde data, the European Centre for Medium-Range Weather Forecasts meteorological analysis fields.

A. Installation

- download the current version of simend2end from <http://www.gfz-potsdam.de/pbl/staff/gbeyerle/tools/index.html>
- create a new directory for simend2end and unzip the archive
- add the new directory to the MATLAB search path
- edit the parameter file 'private/priv_controlparlocal.m' (optional)

B. Usage

The simulation tool is started from the MATLAB command line with

```
>> simend2end( OccNo, TrkType, CN0, Control)
```

The integer 'OccNo' characterizes an occultation event calculated for a specific refractivity profile. The refractivity profile is defined in the parameter file ['simend2endrefrpar_' OccNo '.m']. I.e. for OccNo=17 the file 'simend2endrefrpar_17.m' is called.

Predefined ranges are (see 'priv_initrefrparameter.m')

- 100,000 - 199,999 : radio sonde data
- 200,000 - 299,999 : DWD local model
- 300,000 - 399,999 : planetary boundary layer studies

The integer 'TrkType' determines the type of signal tracking employed. The tracking parameters are defined in the parameter file ['simend2endtrkpar_' TrkType '.m']. I.e. for TrkType=11 the file 'simend2endtrkpar_11.m' is called.

'TrkType'

- 0 : no receiver (no noise is added to signal)
- 2 : closed-loop tracking, no fly-wheeling, 4-quad carrier phase extraction, 3rd order PLL, 30 Hz bandwidth
- 11 : open-loop, with navigation data modulation
- 12 : open-loop, with navigation data modulation, Doppler model shifted by +10 Hz
- 13 : closed-loop, no fly-wheeling, 4-quad phase extraction, 3rd order PLL, 5 Hz bandwidth
- 14 : closed-loop, no fly-wheeling, 4-quad phase extraction, 2nd order PLL, 30 Hz bandwidth
- 15 : closed-loop, fly-wheeling active, 2-quad phase extraction, 3rd order PLL, 30 Hz bandwidth

The float number 'CN0' determines the carrier signal-to-noise density ratio in units of dB Hz; default value is 45 dB Hz.

Parameters controlling the simulation flow can be set with the structure 'Control':

Control.NewA

- 1 : calculate orbit data
- 0 : read orbit from intermediate MAT file

Control.SaveDataA

- 1 : save orbit data to intermediate MAT file
- 0 : don't save

Control.NewB

- 1 : run forward model to calculate bending angle profile
- 0 : read forward model results from intermediate MAT file

Control.SaveDataB

- 1 : save forward model results to intermediate MAT file
- 0 : don't save

Control.NewC

- 1 : run signal tracking and FSI retrieval
- 0 : read simulation results from intermediate MAT file

Control.SaveDataC

- 1 : save simulation results to intermediate MAT file
- 0 : don't save

Control.Visual

- 1 : plot results on screen (default)
- 0 : don't create figures

Control.RandomNoise

- 0 : initialize random generator with 'OccNo' (default)
- 1 : initialize random generator with system time
(results may not be reproducible)

Control.SaveResultsAsASCII

- 1 : write results to file in ASCII format
- 0 : no ASCII output (default)

Control.SondeProfileSmooth

- width of smoothing window applied to sonde refractivity
in meters (default: 150 m)

Further customization is done by setting parameters in

priv_controlparlocal.m : machine/site specific settings
priv_controlpardefault.m : general parameters

Example:

```
>> simend2end( 10010, 15, 45)
```

Calculate refractivity profile AWI radio sonde profile #10, add noise to obtain signal-to-noise density ratio of 45 dB Hz, track with closed-loop fly-wheeling enabled receiver and plot result on screen.

Parameter files

a) Refractivity profile

Information on the refractivity profile is stored in the structure 'RefrPar' comprising the following six fields:

```
RefrPar.pp = spline( Altitude, Refractivity)  
fit parameters derived from a spline fit of a (high resolution)  
refractivity profile as a function of altitude.
```

```
RefrPar.zMin  
lower limit of altitude range [m]
```

```
RefrPar.RefrMin  
refractivity at altitude 'RefrPar.zMin'
```

```
RefrPar.zMax  
upper limit of altitude range [m]
```

```
RefrPar.RefrMax  
refractivity at altitude 'RefrPar.zMax'
```

```
RefrPar.ScaleHeight  
scale height, profile is extrapolated below 'RefrPar.zMin'  
and above 'RefrPar.zMax' with exponential function using a  
scale height of 'RefrPar.ScaleHeight'
```

b) Signal tracking parameters

```
Control.FourQuadExtraction  
1 : four quadrant carrier phase extraction (atan2(Q,I))  
0 : two quadrant carrier phase extraction (atan(Q/I))
```

Control.TrackClosedLoop

- 1 : track in closed-loop mode
- 0 : don't track in closed-loop mode

Control.TrackOpenLoop

- 1 : track in open-loop mode
- 0 : don't track in open-loop mode

Control.OLModelFrqOffset

over-all shift of open-loop Doppler model [Hz]

Control.PLLOrder

loop order employed in closed-loop tracking

Control.LoopBLT

bandwidth of carrier tracking loop times loop update time (1 ms) (i.e. 0.030 corresponds to 30 Hz loop bandwidth)

Control.DataWipeActive

- 1 : 50 Hz navigation data is predicted and removed from signal (data-wipe)
- 0 : don't do data-wipe

Control.CohIntegTime

coherent integration time [s] (default: 0.020)

Control.FlyWheeling

- 0 : fly-wheeling deactivated
- 1 : fly-wheeling activate

Control.FlyWheelDataWipeActive

- 1 : data-wipe during fly-wheeling
- 0 : no data-wipe during fly-wheeling

Control.FlyWheelSNRThreshLo

active fly-wheeling if SNR drops below this value [V/V]

Control.FlyWheelSNRThreshHi

deactive fly-wheeling if SNR rises above this value [V/V]

Control.FlyWheelAvgTime

time period used for NCO frequency extrapolation [s]

Control.FlyWheelDelayAct

delay for activation of fly-wheeling [s]

Control.FlyWheelDelayDeAct

delay for deactivation of fly-wheeling [s]

Control.FlyWheelFourQuadExtr

- 1 : four-quadrant phase extraction during fly-wheeling
- 0 : two-quadrant phase extraction during fly-wheeling

Control.FlyWheelNoResPhase

- 1 : don't add residual phase to NCO phase during fly-wheeling
- 0 : add residual phase to NCO phase during fly-wheeling

Control.FlyWheelPolyDegree

degree of fit polynomial used for extrapolation

Input & output

Intermediate and final results stored in files (binary MATLAB format), default output directory is '`.../simend2end/data/out/mat/`'

The following figures are created with the call to private function '`priv_plotresults.m`'

'Figure 1: SNR':

Signal-to-noise ratio as a function of occultation time

'Figure 3: path difference':

Difference between retrieved and true optical path as a function of occultation time

'Figure 4: residual phase':

Residual phase as a function of occultation time

'Figure 5: Doppler deviation':

Deviation between true and retrieved Doppler as a function of occultation time

'Figure 6: path difference':

Difference between true and retrieved optical path as a function of occultation time

'Figure 7: bending angle':

Bending angle as a function of ray height

blue : true profile

red : retrieved profile

'Figure 8: FSI amplitude':

FSI amplitude as a function of ray height

black : FSI amplitude

green : smoothed amplitude

red : cut-off ray height

'Figure 9: refractivity':
Refractivity as a function of altitude
red : true profile
blue : retrieved profile

'Figure 10: refractivity gradient':
Refractivity gradient as a function of altitude
red : true profile
blue : retrieved profile

'Figure 11: refractivity error':
Fractional deviation between true and retrieved
refractivity as a function of altitude.

C. License

SIMEND2END --- An end-to-end radio occultation simulator

Copyright (C) 2000-2005 Georg Beyerle

This program is free software; you can redistribute it and/or modify it under the terms of the GNU General Public License as published by the Free Software Foundation; either version 2 of the License, or (at your option) any later version.

This program is distributed in the hope that it will be useful, but WITHOUT ANY WARRANTY; without even the implied warranty of MERCHANTABILITY or FITNESS FOR A PARTICULAR PURPOSE. See the GNU General Public License for more details.

You should have received a copy of the GNU General Public License along with this program; if not, write to the Free Software Foundation, Inc., 51 Franklin Street, Fifth Floor, Boston, MA 02110-1301, USA